

Learning Proximal Operators to Discover Multiple Optima

Lingxiao Li^{*1}, Noam Aigerman², Vladimir G. Kim², Jiajin Li³, Kristjan Greenewald⁴,
Mikhail Yurochkin⁴, and Justin Solomon¹

¹MIT

²Abofe Research

³Stanford University

⁴MIT-IBM Watson AI Lab

Abstract

Finding multiple solutions of non-convex optimization problems is a ubiquitous yet challenging task. Typical existing solutions either apply single-solution optimization methods from multiple random initial guesses or search in the vicinity of found solutions using ad hoc heuristics. We present an end-to-end method to learn the proximal operator across a family of non-convex problems, which can then be used to recover multiple solutions for unseen problems at test time. Our method only requires access to the objectives without needing the supervision of ground truth solutions. Notably, the added proximal regularization term elevates the convexity of our formulation: by applying recent theoretical results, we show that for weakly-convex objectives and under mild regularity conditions, training of the proximal operator converges globally in the over-parameterized setting. We further present a benchmark for multi-solution optimization including a wide range of applications and evaluate our method to demonstrate its effectiveness.

1 Introduction

Searching for multiple solutions of an optimization problem is a ubiquitous but under-explored task. On the one hand, searching for a globally optimal solution in a nonconvex landscape typically involves starting with multiple initial guesses, optimizing each guess independently to reach a local minimum, and choosing the candidate solution with the smallest objective. On the other hand, in applications like low-rank recovery [Ge et al., 2017], topology optimization [Papadopoulos et al., 2021], object detection [Lin et al., 2014], and symmetry detection [Shi et al., 2020], it is desirable to recover multiple near-optimal solutions, either because there are multiple equally-performant global optima or due to the fact that the optimization objective does not capture user preferences precisely. Orthogonally, it is common for an optimization problem to have parameters whose values are not known in advance, for instance, the weight of a regularization term. Then, it is in the user’s interest to be able to quickly obtain solutions with different parameters without having to restart from scratch.

Formalizing these concerns, we define a *multi-solution optimization* (MSO) problem to be the minimization $\min_{x \in \mathcal{X}} f_\omega(x)$, where $\omega \in \Omega$ is the parameter of the problem, \mathcal{X} is the search space of the variable x , and $f_\omega : \mathbf{R}^d \rightarrow \mathbf{R}$ is the objective function depending on ω . The goal of MSO is to identify multiple solutions for each $\omega \in \Omega$, e.g., the set $\{x^* \in \mathcal{X} : f_\omega(x^*) = \min_{x \in \mathcal{X}} f_\omega(x)\}$, which can contain more than one element or even infinitely many elements. In this work, we assume that $\mathcal{X} \subset \mathbf{R}^d$ where d is small, and that Ω is, in a loose sense, a continuous space, such that the objective f_ω changes continuously as ω varies. To make gradient-based methods viable, we further assume that each f_ω is

^{*}Corresponding author. Email: lingxiao@mit.edu

differentiable almost everywhere with respect to x . As finding all global minima in the general case is extremely challenging, realistically our goal is to find a diverse set of local optima.

As an example, for object detection, Ω could parameterize the space of images and \mathcal{X} could be the 4-dimensional space of bounding boxes (ignoring class labels). Then, $f_\omega(x)$ could be a loss function that measures how close the bounding box x is to being one of the ground truth boxes. Solving MSO given f_ω 's would yield *all* object bounding boxes (Section 5.5).

If we have a training dataset of parameters ω 's with annotated ground truth solutions such as in the setting of multi-label learning [Tsoumakas and Katakis, 2007], then supervised learning can solve MSO by predicting a fixed number of solutions with confidence scores, using a set-based loss that measures whether all ground truth solutions have been recovered [Huttenlocher et al., 1993, Liu et al., 2010, Frogner et al., 2015]. Unfortunately, such annotation is not available for most optimization problems in the wild. If we fix ω , a naïve approach is to initialize a finite number of particles randomly in \mathcal{X} and then optimize each particle independently using a gradient-based optimizer. However, this can be costly if many particles are needed, and we might have to repeat the process for every ω .

In this work, we propose an end-to-end method that approximates the **proximal operator** of an MSO objective function using a neural network. Intuitively, the proximal operator runs a single step of the **proximal-point algorithm** on an input point, making local improvement without moving too far from the input. Repeated application of the proximal operator pushes an input point to a nearby local optimum. The proximal-point algorithm is known to converge faster than gradient descent, both empirically and theoretically, even when the proximal operator is approximated Rockafellar [1976, 2021], Hoheisel et al. [2020]. Such fast convergence motivates us to *learn* the proximal operator so that once learned the operator only needs to be applied a few times to push an input to a nearby local optimum. Probabilistically, the learned proximal operator implicitly encodes the solutions of an MSO problem as the pushforward of a prior distribution by iterated application of the operator. This representation bypasses the need to predict a fixed number of solutions and can represent infinitely many solutions. We further allow the learned proximal operator to generalize to different problem parameters by treating ω as an input to the network along with an application-specific encoder.

To train the proximal operator, we optimize a straightforward loss term including only the objective plus an ℓ^2 -type *proximal term* that prevents a point from moving too far away. Remarkably, such proximal term promotes the convexity of the formulation: applying recent theoretical results [Kawaguchi and Huang, 2019], we show that for weakly-convex objectives that are sufficiently regular, the training converges globally so long as the total number of network weights is at least linear in the size of the training data.

Literature on MSO is scarce, so we build a benchmark with a wide variety of applications including level set sampling, non-convex sparse recovery, max-cut, 3D symmetry detection, and object detection in images. When evaluated on this benchmark, our learned proximal operator reliably produces high-quality results compared to reasonable alternatives, while converging in few iterations.

2 Related Works

Learning to optimize. Learning to optimize (L2O) applies deep learning to learn from past optimization experience to optimize future problems more effectively and faster; see [Chen et al., 2021] for a survey. *Model-free* L2O uses recurrent neural networks to discover new optimizers suitable for similar problems [Andrychowicz et al., 2016, Li and Malik, 2016]. In comparison, we learn a problem-dependent proximal operator so that at test time we do not need access to objective functions or their gradients, which can be costly to evaluate (e.g. symmetry detection in Section 5.4) or unavailable (e.g. object detection in Section 5.5). *Model-based* L2O substitutes components of a specialized optimization framework or schematically unrolls an optimization procedure with neural networks. Related to proximal methods, Gregor and LeCun [2010] emulate a few iterations of proximal gradient descent using neural networks for sparse recovery with an ℓ^1 regularizer, extended to non-convex regularizers by Yang et al. [2020]. Meinhardt et al. [2017] use a fixed denoising neural network as a surrogate proximal operator

for inverse imaging problems. These works use schematics of proximal methods to design a neural network that is then trained with strong supervision. In contrast, we learn the proximal operator directly, requiring only access to the objectives; we do not need ground truth for inverse problems.

Finding multiple solutions. Brits et al. [2007] introduce *niching* to particle swarm optimization to discover multiple optima in multi-modal optimization. Li [2009] mitigates the difficulty of tuning niching parameters using a ring neighborhood topology. Larson and Wild [2018] propose a parallel multi-start algorithm that applies local optimization on promising sample points. These methods require complicated handcrafted heuristics and do not generalize to unseen but similar problems. Papadopoulos et al. [2021] develop a deflation method for topology optimization to find multiple solutions of a PDE. Yet the exploration of the search space is slow, as only one new solution is discovered before modifying and solving the system.

Predicting multiple solutions is universal in deep learning tasks like multi-label classification [Tsoumakas and Katakis, 2007] and detection [Liu et al., 2020]. The typical solution is to ask the network to predict a fixed number of candidates along with confidence scores to indicate how likely each candidate is to be a solution [Ren et al., 2015, Li et al., 2019, Carion et al., 2020]. Then the solutions will be chosen from the candidates using heuristics such as non-maximum suppression [Neubeck and Van Gool, 2006]. Models that output a fixed number of solutions without taking into account the unordered set structure can suffer from discontinuity Zhang et al. [2019]. Moreover, this approach cannot handle the case when the solution set is continuous.

Multi-objective optimization. A related general problem is multi-objective optimization (MOO) [Deb, 2014], where the goal is to discover a Pareto set in which no solution is better than any other in all objectives. While many recent works in MOO focus on recovering a single solution in the Pareto set given a preference vector of the objectives [Lin et al., 2019, Mahapatra and Rajan, 2020, Navon et al., 2020], a few methods propose searching along the tangent space of a Pareto set point to discover nearby points in the Pareto set based on first-order approximation [Hillermeier, 2001, Schulz et al., 2018, Ma et al., 2020] but with no guarantee on the exhaustiveness of such random exploration. Even for a single objective, as we will show, finding multiple solutions is already meaningful.

Deep ensembles. Finding multiple solutions along an optimization trajectory of a deep learning model yields an ensemble of neural networks from which we can obtain models with improved accuracy, uncertainty, and out-of-distribution robustness. Such ensembles can be generated by, for example, instantiating multiple neural networks using weights from different optimization epochs [Xie et al., 2013] or temporarily increasing the learning rate after a solution is found to jump to a different one [Huang et al., 2017, Garipov et al., 2018]. However, these ensembling strategies are likely to leave larger portions of the solution space unexplored: Fort et al. [2019] argue that training individual neural networks using random initialization more effectively explores the modes of the loss landscape, whereas methods based on an optimization trajectory tend to produce clustered ensembles. Our method is a computationally more efficient alternative to the random initialization strategy: during training and testing, random batches of trajectories are formed by iteratively applying the proximal operator to sampled points in order to efficiently explore the optimization landscape.

Wasserstein gradient flow. Pushing forward a probability distribution by the proximal operator corresponds to one step of the JKO scheme for Wasserstein gradient flow of a linear functional in the space of distributions [Jordan et al., 1998, Benamou et al., 2016]. Compared to recent works on neural Wasserstein gradient flow [Mokrov et al., 2021, Hwang et al., 2021, Bunne et al., 2021], where a separate network is needed to parameterize the pushforward map for every JKO step, our linear functional yields a pushforward map that is identical for each step; this property allows us to use a single neural network as a parameterization.

3 Method

We tackle MSO by learning the proximal operator of the corresponding objective, minimizing a loss similar to the definition of the proximal operator.

3.1 Preliminaries

Given the objective $f_\omega : \mathbf{R}^d \rightarrow \mathbf{R}$ of an MSO problem parameterized by ω , the corresponding **proximal operator** [Moreau, 1962, Rockafellar, 1976, Parikh and Boyd, 2014] is defined for a fixed $\lambda \in \mathbf{R}_{>0}$ as

$$\text{prox}(x; \omega) := \arg \min_y \left\{ f_\omega(y) + \frac{\lambda}{2} \|y - x\|_2^2 \right\}. \quad (1)$$

The weight λ in front of the proximal term¹ controls how close $\text{prox}(x; \omega)$ is to x : increasing λ will reduce $\|\text{prox}(x; \omega) - x\|_2$. For the $\arg \min$ in (1) to be unique, a sufficient condition is that f_ω is ξ -weakly convex with $\xi < \lambda$, so that $f_\omega(y) + \frac{\lambda}{2} \|y - x\|_2^2$ is strongly convex. The class of weakly convex functions is deceptively broad: for instance, any C^2 function on a compact convex set is weakly convex. In this case, $\text{prox}(x; \omega)$ is precisely one step of the backward Euler discretization of integrating the vector field $-\nabla f_\omega$ with time step $1/\lambda$ [Parikh and Boyd, 2014].

The **proximal-point algorithm** (PPA) for finding a local minimum of f_ω iterates

$$x^k := \text{prox}(x^{k-1}; \omega), \forall k \in \mathbf{N}_{\geq 1},$$

with initial point x^0 Rockafellar [1976]. In practice, $\text{prox}(x; \omega)$ often can only be approximated, resulting in *inexact* PPA. When the objective function is locally indistinguishable from a convex function and x^0 is sufficiently close to the set of local minima, then with reasonable stopping criterion, inexact PPA can converge linearly to a local minimum of the objective: the smaller λ is, the faster the convergence rate becomes [Rockafellar, 2021].

3.2 Learning Proximal Operators

The fast convergence rate of PPA makes it a good candidate for MSO: to obtain a diverse set of solutions for any $\omega \in \Omega$, we can run a few iterations of PPA from diverse initial points. The proximal term penalizes big jumps and prevents points from collapsing to a single solution. However, running a subroutine to approximate $\text{prox}(x; \omega)$ for every pair (x, ω) can be costly.

To overcome this issue, we *learn* the operator $\text{prox}(\cdot; \cdot)$ given access to $\{f_\omega\}_{\omega \in \Omega}$. A naïve way to learn $\text{prox}(\cdot; \cdot)$ is to first solve (1) to produce ground truth for a large number of (x, ω) pairs independently using gradient-based methods and then learn the operator using mean-squared error loss. However, this approach is costly as the space $\mathcal{X} \times \Omega$ can be large. Moreover, this procedure requires a stopping criterion for the minimization in (1) which is hard to design *a priori*.

Instead, we formulate the following end-to-end optimization over the space of functions:

$$\min_{\Phi: \mathcal{X} \times \Omega \rightarrow \mathcal{X}} \mathbf{E}_{x \sim \mu, \omega \sim \nu} \left[f_\omega(\Phi(x, \omega)) + \frac{\lambda}{2} \|\Phi(x, \omega) - x\|_2^2 \right], \quad (2)$$

where x is sampled from μ , a distribution on \mathcal{X} , and ω is sampled from ν , a distribution on Ω . To get (2) from (1), we essentially substitute y with the output $\Phi(x, \omega)$ and integrate over the product probability distribution $\mu \otimes \nu$.

To solve (2), we parameterize $\Phi : \mathcal{X} \times \Omega \rightarrow \mathcal{X}$ using a neural network with additive and multiplicative residual connections (Appendix B). Intuitively, the implicit regularization of neural networks aligns well with the regularity of $\text{prox}(\cdot; \cdot)$: for a fixed ω the proximal operator $\text{prox}(\cdot; \omega)$ is 1-Lipschitz in local regions where f_ω is convex, while as the parameter ω varies $\text{prox}(x; \omega)$ should not change too much. To make (2) computationally practical during training, we realize ν as a training dataset and choose μ to be the uniform distribution on \mathcal{X} . To train Φ , we sample a mini-batch of (x, ω) to evaluate the expectation and optimize using Adam [Kingma and Ba, 2014]. For problems where the space Ω is structured (e.g. with images or point clouds), we first embed ω into a Euclidean feature space through an application-specific encoder before passing it to Φ . This allows us to use efficient domain-specific encoder (e.g., convolutional networks) to promote generalization to unseen ω .

¹A usual convention is to use the reciprocal of λ in front of the proximal term.

3.3 Extracting Solutions

To extract multiple solutions at test time for a problem with parameter ω , we sample a batch of x 's from μ and then apply the learned $\Phi(\cdot, \omega)$ to each sample a few times. Each application of Φ approximates a single proximal step on the samples. From a distributional perspective, for $k \in \mathbf{N}_{\geq 0}$, we can view Φ^k —the operator Φ applied k times—as a generative model so that the pushforward distribution, $(\Phi^k)_\# \mu$, approximates the distribution obtained after k proximal steps. An advantage of our representation is that it can represent arbitrary number of solutions (Figure C.5) and can handle the case when the solution set is continuous (Figure C.2). This highlights the difference between our setup and that of existing L2O methods [Chen et al., 2021]: at test time, we do not need access to $\{f_\omega\}_{\omega \in \Omega}$ or their gradients, which can be costly to evaluate or unavailable; instead we only need ω (e.g. in the case of object detection, ω is an image).

3.4 Convergence of Training

We have turned the problem of finding multiple solutions for each f_ω in the space \mathcal{X} into the problem of finding a single solution for (2) in the space of functions. If the f_ω 's are ξ -weakly convex with $\xi < \lambda$ and $\text{supp } \mu = \mathcal{X}$, $\text{supp } \nu = \Omega$, then the solution of (2) is the unique proximal operator with corresponding λ .

If in addition the gradients of the objectives are Lipschitz, using recent learning theory results [Kawaguchi and Huang, 2019] we can show that with practical degrees of over-parameterization, gradient descent on neural network parameters of Φ converges globally during training. Suppose our training dataset is $S = \{(x_i, \omega_i)\}_{i=1}^n \subset \mathcal{X} \times \Omega$. Define the training loss, a discretized version of (2) using S , to be, for $g : \mathcal{X} \times \Omega \rightarrow \mathcal{X}$,

$$L(g) := \frac{1}{n} \sum_{i=1}^n \left[f_{\omega_i}(g(x_i, \omega_i)) + \frac{\lambda}{2} \|g(x_i, \omega_i) - x_i\|_2^2 \right]. \quad (3)$$

Theorem 3.1 (informal). *Suppose for any $\omega \in \Omega$, the objective f_ω is differentiable, ξ -weakly convex, and ∇f_ω is ζ -Lipschitz with $\xi \leq \lambda$. Then for any feed-forward neural network with $\tilde{\Omega}(n)$ total parameters and common activation units, when the initial weights are drawn from random Gaussians, with high probability, gradient descent on its weights using a fixed learning rate will eventually reach minimum loss $\min_{g: \mathcal{X} \times \Omega \rightarrow \mathcal{X}} L(g)$ where the number of iterations needed to achieve $\epsilon > 0$ error is $O((\lambda + \zeta)/\epsilon)$.*

We state and prove Theorem 3.1 formally Appendix A. Even though the optimization over network weights is non-convex, training can still result in a globally minimal loss.

We note a few gaps between Theorem 3.1 and our implementation. First, we use SGD with mini-batching instead of gradient descent. Second, instead of feed-forward networks, we use a network architecture with residual connections (Figure B.1), which works better empirically. Under these conditions, global convergence results can still be obtained, e.g. via [Allen-Zhu et al., 2019, Theorems 6 and 8], but with large polynomial bounds in n, H for the network parameters. Another gap is caused by the restriction of the function class of the objectives. In several applications in Section 5, the objective functions are not weakly convex or we deliberately choose small λ for faster PPA convergence; we empirically demonstrate that our method remains effective.

In Figure C.1 we empirically verify that when the objective is the ℓ^1 norm, the trained operator converges to the true proximal operator, the shrinkage operator, in the L^2 sense.

3.5 Importance Sampling via Unfolding PPA

Directly optimizing (2) using mini-batching may not yield an operator that can refine a near-optimal solution, as the expectation is taken over a uniform measure μ . Ideally, we would like to sample from a distribution that puts more probability on near-optimal solutions. We achieve this goal as follows, inspired by Wang and Solomon [2019].

Let Ψ denote the network with weights after l training iterations. Denote $\mu^k := (\Psi^k)_\#(\mu)$. For $K \in \mathbf{N}_{\geq 1}$, define $\tilde{\mu}^K := \frac{1}{K} \sum_{k=1}^K \mu^k$. Compared to μ , the new measure $\tilde{\mu}^K$ is more concentrated in near-optimal regions as l increases. Then, for training iteration $l+1$, we optimize the following objective function obtained by replacing μ by $\tilde{\mu}^K$ in (2):

$$\mathbf{E}_{\substack{x \sim \tilde{\mu}^K \\ \omega \sim \nu}} \left[f_\omega(\Phi(x, \omega)) + \frac{\lambda}{2} \|\Phi(x, \omega) - x\|_2^2 \right]. \quad (4)$$

In practice, we choose $K = 5$ or $K = 10$. For the choice of other hyper-parameters, see Appendix C.1.

4 Performance Measures

In this section, we propose metrics for MSO to evaluate our method, a way to generate ground truth, and a baseline method for comparison.

4.1 Metrics

Designing a single-valued metric for MSO is challenging since one needs to consider the diversity of the solutions as well each solution’s level of optimality. For an MSO problem with parameter ω and objective f_ω , the output of an MSO algorithm can be represented as a (possibly infinite) set of solutions $\{x_\alpha\}_\alpha \subset \mathcal{X}$ with objective values $u_\alpha := f_\omega(x_\alpha)$. Suppose we have access to ground truth solutions $\{y_\beta\}_\beta \subset \mathcal{X}$ with $v_\beta := f_\omega(y_\beta)$. Pick a threshold $t \in \mathbf{R}$ and denote $A_t := \{x_\alpha : u_\alpha \leq t\}$, $B_t := \{y_\beta : v_\beta \leq t\}$. That is, A_t, B_t contain solutions with objectives no worse than t . Let μ be a uniform measure on the bounded search space \mathcal{X} and draw $W \sim \mu$. Define a random variable

$$D_t := \frac{1}{2} \left\| \text{proj}_{A_t}(W) - \text{proj}_{B_t}(\text{proj}_{A_t}(W)) \right\|_2 + \frac{1}{2} \left\| \text{proj}_{B_t}(W) - \text{proj}_{A_t}(\text{proj}_{B_t}(W)) \right\|_2, \quad (5)$$

where $\text{proj}_S(x) := \arg \min_{s \in S} \|x - s\|_2$. We call W a *witness* of D_t , as it witnesses how different A_t and B_t are near W . To describe the law of D_t , we define the *witnessed divergence* and *witnessed precision* at $\delta > 0$ as

$$\text{WD}_t := \mathbf{E}[D_t] \quad \text{and} \quad \text{WP}_t^\delta := \mathbf{P}(D_t < \delta). \quad (6)$$

Witnesses help handle unbalanced clusters that can appear in the solution sets. These metrics are agnostic to duplicates, unlike the chamfer distance or optimal transport metrics. Compared to alternatives like the Hausdorff distance, WD_t remains low if a small portion of A_t, B_t are mismatched (Figure 1). One can interpret WD_t as a weighted chamfer distance whose weight is proportional to the volume of the ℓ^2 -Voronoi cell at each point in either point cloud.

4.2 Particle Descent: Ground Truth Generation

A straightforward method for MSO is to spawn many particles in \mathcal{X} , for each $\omega \in \Omega$, and to perform gradient descent on the particles independently. We use this method to generate ground truth solutions used to compute the metrics in (6) whenever the ground truth is not available. We use Adam as an optimizer [Kingma and Ba, 2014]. Note this method is not directly comparable to ours because it cannot generalize to unseen ω ’s at test time. Remarkably, for highly non-convex objectives, particle descent can produce worse solutions than the ones obtained using the learned proximal operator (Figure C.6).

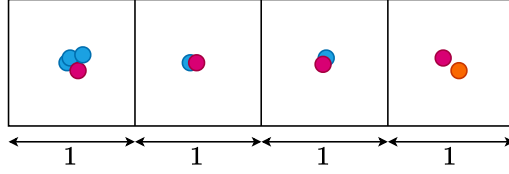


Figure 1: Illustration of witness metrics. In this example, when computing the witness metrics between the red and blue points, we have $\mathbf{P}(D_t \approx 0) = 3/4$ and $\mathbf{P}(D_t \approx 0.5) = 1/4$. D_t is only non-vanishing when W is in the rightmost square. This aligns well with the intuition that $3/4$ of the red points match with the blue ones. In comparison, the Hausdorff distance between the red points and the blue points is about 1, which is the same as the Hausdorff distance between the orange point and the blue point, despite the fact most of red points are close to the blue ones.

4.3 Learning Gradient Descent Operators

As there is no readily-available application-agnostic baseline for MSO, we propose the following method that learns iterations of the gradient descent operator. Fix $Q \in \mathbf{N}_{\geq 1}$ and a step size $\eta > 0$. We optimize an operator Ψ via

$$\min_{\Psi: \mathcal{X} \times \Omega \rightarrow \mathcal{X}} \mathbf{E}_{x \sim \mu, \omega \sim \nu} \|\Psi(x, \omega) - \text{gd}(x, Q; \omega)\|_2^2, \quad (7)$$

where $\text{gd}(x, Q; \omega)$ is the result of Q steps of gradient descent on f_ω starting at x , i.e., $\text{gd}(x, 0; \omega) = x$, and $\text{gd}(x, k; \omega) = \text{gd}(x, k-1; \omega) - \eta \nabla f_\omega(\text{gd}(x, k-1; \omega))$. Computing the loss (7) requires Q evaluations of ∇f_ω , which can be costly (e.g., for symmetry detection in Section 5.4). We set $Q = 10$ in all experiments except for symmetry detection, where we use $Q = 1$. We use importance sampling similar to Section 3.5. An ODE interpretation is that Ψ performs k iterations of *forward* Euler on the gradient field ∇f_ω , whereas the learned proximal operator performs a single iteration of *backward* Euler. As we will see in Figure C.5, this approach struggles with non-smooth objectives due to the fixed step size, while the learned proximal operator has no such issues.

5 Applications

We consider five applications to benchmark our MSO method, chosen to highlight the ubiquity of MSO in diverse settings. We abbreviate POL for proximal operator learning (proposed method), GOL for gradient operator learning (Section 4.3), and PD for particle descent (Section 4.2).

5.1 Sampling from Level Sets

Formulation. Level sets provide a concise and resolution-free implicit shape representation suitable for learning applications [Museth et al., 2002, Park et al., 2019, Sitzmann et al., 2020]. Yet they are less intuitive to work with, even for straightforward tasks on discretized domains (meshes, point clouds) like visualizing or integrating over a level set. We present an MSO formulation to sample from level sets, enabling adaptation of downstream tasks to level sets.

Given a family of functions $\{g_\omega : \mathcal{X} \rightarrow \mathbf{R}^q\}_{\omega \in \Omega}$, for each ω suppose we want to sample from the 0-level set $g_\omega^{-1}(0)$. We formulate an MSO problem with objective $f_\omega(x) := \|g_\omega(x)\|_2^2$, whose global optima are precisely $g_\omega^{-1}(0)$. We do not need assumptions on level set topology or that the implicit function represents a distance field [Park et al., 2019, Deng et al., 2020, Chen et al., 2020].

Benchmark. We consider sampling from conic sections. Let $\mathcal{X} = [-5, 5]^2$ and $\Omega = [-1, 1]^6$. For $\omega = (A, B, C, D, E, F) \in \Omega$, define g_ω to be

$$g_\omega(x_1, x_2) := Ax^2 + Bxy + Cy^2 + Dx + Ey + F.$$

Since $f_\omega = (g_\omega)^2$ is defined on a compact \mathcal{X} , it satisfies the conditions of Theorem 3.1 for a large λ , but a large λ corresponds to small PPA step size. Experimentally, small λ for POL gave decent

results compared to GOL: Figure 2 illustrates that POL consistently produces sharper level sets for both hyperbolas ($B^2 - 4AC > 0$) and ellipses ($B^2 - 4AC < 0$). Figure C.3 shows that POL yields significantly higher WP_t^δ than GOL for small δ , implying that details are well recovered. Figure C.4 verifies that iterating the trained operator of POL converges much faster than that of GOL.

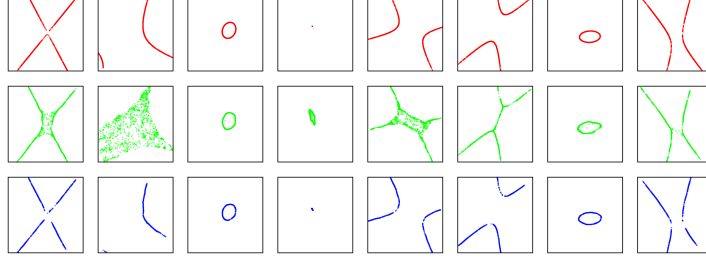


Figure 2: Visualization of the solutions for the conic section problem. Red, green, and blue indicate the solutions by PD, GOL, and POL respectively. See Figure C.2 for more examples.

5.2 Sparse Recovery

Formulation. In signal processing, the *sparse recovery* problem aims to recover a signal $x^* \in \mathcal{X} \subset \mathbf{R}^d$ from a noisy measurement $y \in \mathbf{R}^m$ distributed according to $y = Ax^* + e$, where $m < d$, $A \in \mathbf{R}^{m \times d}$, and e is measurement noise Beck and Teboulle [2009]. In applications like imaging and speech recognition, the signals are *sparse*, with few non-zero entries [Marques et al., 2018]. Hence, the goal of sparse recovery is to recover a sparse x^* given A and y .

A common way to encourage sparsity is to solve least-squares plus an ℓ^p norm on the signal:

$$\min_{x \in \mathcal{X}} \frac{1}{2} \|Ax - y\|_2^2 + \alpha \|x\|_p^p, \quad (8)$$

for $\alpha, p > 0$ and $\|x\|_p^p := \sum_{i=1}^d (x_i^2 + \epsilon)^{p/2}$ for a small ϵ to prevent instability. We consider the non-convex case where $0 < p < 1$. Compared to convex alternatives like LASSO ($p = 1$), non-convex ℓ^p norms require milder conditions under which the global optima of (8) are the desired sparse x^* [Chartrand and Staneva, 2008, Chen and Gu, 2014].

To apply our MSO framework, we define $\omega = (\alpha, p) \in \Omega$ and f_ω to be the objective (8) with corresponding α, p . Compared to existing methods for non-convex sparse recovery [Lai et al., 2013], our method can recover multiple solutions from the non-convex landscape for a family of α, p 's without having to restart. The user can adjust parameters α, p to quickly generate candidate solutions and then choose a solution based on their preference.

Benchmark. Let $\mathcal{X} = [-2, 2]^8$, $\Omega = [0, 1] \times [0.2, 0.5]$. We consider highly non-convex ℓ^p norms with $p \in [0.2, 0.5]$ to test our method's limits. We choose $d = 8$ and $m = 4$, and sample the sparse signal x^* uniformly in \mathcal{X} . We then sample entries in A i.i.d. from $\mathcal{N}(0, 1)$ and generate $y = Ax^* + e$ where $e \sim \mathcal{N}(0, 0.1)$. Although $\|x\|_p^p$ is not weakly convex, POL achieves decent results (Figure C.5). Remarkably, POL often reaches a better objective than PD (Figure C.6) while retaining diversity, even though POL uses a much bigger step size ($1/\lambda = 0.1$ compared to PD's 10^{-5}) and needs to learn a different operator for an entire family of $\omega \in \Omega$.

5.3 Rank-2 Relaxation of Max-Cut

Formulation. MSO can be applied to solve combinatorial problems that admit smooth non-convex relaxations. Here, we consider the classical problem of finding the maximum cut of an undirected graph $G = (V, E)$, where $V = \{1, \dots, n\}$, $E \subset V \times V$, with edge weights $\{w_{ij}\} \subset \mathbf{R}$ so that $w_{ij} = 0$ if $(i, j) \notin E$. The goal is to find $\{x_i\} \in \{-1, +1\}^V$ to maximize $\sum_{i,j} w_{ij}(1 - x_i x_j)$.

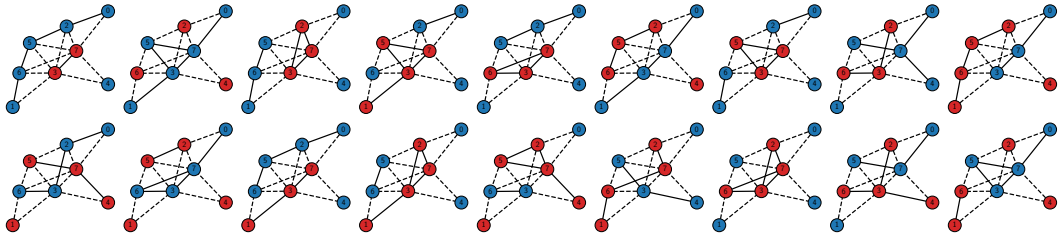


Figure 3: 18 different max cuts (max cut value 10) of a graph generated by our method. Red and blue vertices indicate the two vertex set separated by the cut. Vertex 0 is set to blue to remove the duplicates obtained by swapping the colors. See Figure C.9 for more results.

Burer et al. [2002] propose the following rank-2 non-convex relaxation of the max-cut problem:

$$\min_{\theta \in \mathbf{R}^n} \sum_{i,j} w_{ij} \cos(\theta_i - \theta_j). \quad (9)$$

The objective (9) inherits weak convexity from cosine, so it satisfies the conditions of Theorem 3.1. Let Ω be the space of all edge weights with n vertices. Instead of using angles as the variables which are ambiguous up to 2π , we represent each variable as a point on the unit circle, so $\mathcal{X} = (S^1)^n$. For $\omega = (\omega_{ij}) \in \Omega$, we define, for $x \in \mathcal{X}$,

$$f_{\omega}(x) = \sum_{i,j} \omega_{ij} x_i^{\top} x_j. \quad (10)$$

After solving (10), we can find cuts using a Goemans and Williamson-type procedure (1995). Instead of using heuristics to find optima near a solution [Burer et al., 2002], our method can help the user effortlessly explore the set of near-optimal solutions without hand-designed heuristics.

Benchmark. We apply our formulation to K_8 , the complete graph with 8 vertices. Hence $\mathcal{X} = (S^1)^8 \subset \mathbf{R}^{16}$. We choose $\Omega = [0, 1]^{28}$ as there are 28 edges in K_8 . We mix two types of random graphs with 8 vertices in training and testing: Erdős-Rényi graphs with $p = 0.5$ and K_8 with uniform edge weights in $[0, 1]$. Figure 3 shows that POL can generate diverse set of max cuts. Quantitatively, compared to GOL, POL achieves better witnessed metrics (Figure C.7).

5.4 Symmetry Detection of 3D Shapes

Formulation. Geometric symmetries are omnipresent in natural and man-made objects. Knowing shape symmetries can benefit downstream tasks in geometry processing and vision Mitra et al. [2013], Shi et al. [2020], Zhou et al. [2021]. We consider the problem of finding all reflection symmetries of a 3D surface. Let ω be a shape representation (e.g. point cloud, multi-view scan), and let $\mathcal{M}_{\omega} \subset \mathbf{R}^3$ denote the corresponding surface mesh. As reflections are determined by the reflectional plane, we set $\mathcal{X} = S^2 \times \mathbf{R}_{\geq 0}$, where $x = (n, d) \in \mathcal{X}$ denotes the plane with normal $n \in S^2 \subset \mathbf{R}^3$ and intercept $d \in \mathbf{R}_{\geq 0}$. We assume $d \geq 0$ to remove the ambiguity of $(-n, -d)$ representing the same plane. Let $R_x : \mathbf{R}^3 \rightarrow \mathbf{R}^3$ denote the corresponding reflection. Perfect symmetries of \mathcal{M}_{ω} satisfy $R_x(\mathcal{M}_{\omega}) = \mathcal{M}_{\omega}$.

Let $s_{\omega} : \mathbf{R}^3 \rightarrow \mathbf{R}$ be the (unsigned) distance field of \mathcal{M}_{ω} given by $s_{\omega}(p) = \min_{q \in \mathcal{M}_{\omega}} \|p - q\|_2$. Inspired by Podolak et al. [2006], we define the MSO objective to be

$$f_{\omega}(x) := \mathbf{E}_{p \sim \mathcal{M}_{\omega}} [s_{\omega}(R_x(p))], \quad (11)$$

where a batch of p is sampled uniformly from \mathcal{M}_{ω} when evaluating the expectation. Although f_{ω} is stochastic, since we use point-to-mesh distances to compute s_{ω} , perfect symmetries will make (11) zero with probability one. Compared to existing learning-based methods [Gao et al., 2020, Shi et al., 2020], our method applied to (11) finds arbitrary numbers of symmetries including continuous ones, without needing ground truth symmetries as supervision.

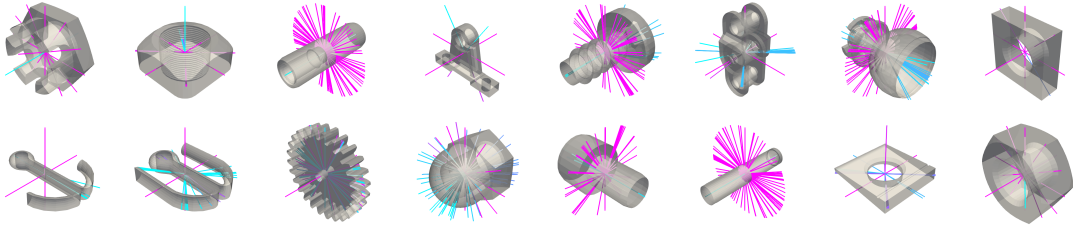


Figure 4: Symmetry detection results using our method. Each reflection is represented as a colored line segment representing the normal of the reflection plane with one endpoint on the plane. Pink indicates better objective values, while blue indicates worse. Our method is capable of detecting complicated discrete symmetries as well as continuous families of reflectional symmetries for cylindrical objects.

Benchmark. We detect reflection symmetries for mechanical parts in the MCB dataset [Kim et al., 2020]. In this case, Ω is the space of 3D point clouds representing mechanical parts. We sample 2048 points with their normals uniformly from each shape and use Wang et al. [2019] to encode the oriented point clouds. Figure 4 visualizes our method’s results on a sample of models; for per-iteration PPA results, see Figure C.10. Figure C.8 shows that POL achieves much higher witnessed precision compared to GOL.

5.5 Object Detection in Images

Formulation. Identifying objects in an image is a central problem in vision on which recent works have made significant progress [Ren et al., 2015, Carion et al., 2020, Liu et al., 2021].

We consider a simplified task where we drop the class labels and predict only object bounding boxes. Let $b = (x, y, w, h) \in \mathcal{X} = [0, 1]^4$ denote a box with (normalized) center coordinates (x, y) , width w , and height h . We choose Ω to be the space of images. Suppose an image ω has K_ω ground truth bounding boxes $\{b_i^\omega\}_{i=1}^{K_\omega}$. We define the MSO objective to be

$$f_\omega(x) = \min_{i=1}^{K_\omega} \|b_i^\omega - x\|_1. \quad (12)$$

The minimizers of (12) are exactly $\{b_i^\omega\}_{i=1}^{K_\omega}$. Although (12) may seem trivial, its gradients reveal the ℓ^1 -Voronoi diagram formed by b_i^ω ’s when training the proximal operator. Different from existing approaches, we encode the predicted boxes in the learned proximal operator without needing to predict confidence scores or a fixed number of boxes.

Benchmark. We apply the above MSO formulation to the COCO2017 dataset [Lin et al., 2014]. See Appendix C.7 on details of data preparation. As ω is an image, we fine-tune ResNet-50 [He et al., 2016] to encode ω into a vector z that can be consumed by the operator network (Figure B.1). Both networks are trained together in an end-to-end fashion.

Figure 5 visualizes 4 iterations of PPA using the learned proximal operator: randomly initialized boxes are quickly refined to form distinctive clusters on detected objects. Figure C.11 shows our object detection results on a large number of randomly chosen test images. Table 1 compares the proposed methods with alternatives and the highly-optimized Faster R-CNN Ren et al. [2015] on our test dataset using witnessed and precision/recall metrics. Since we do not output confidence scores, the metrics are computed solely based on the set of predicted boxes; see Section 5.5 for details. In addition to GOL, we design a baseline method FN that uses the same ResNet-50 backbone and predicts a fixed number of boxes using the chamfer distance as the training loss.

Our method achieves significantly better results than FN and GOL. Compared to the Faster R-CNN, we achieve slightly worse results with 40.7% fewer network parameters. In particular, the proximal operator network is only 1.65MB (excluding the ResNet-50 encoder). While Faster R-CNN contains highly-specialized modules such as the regional proposal network, in our method we simply feed the

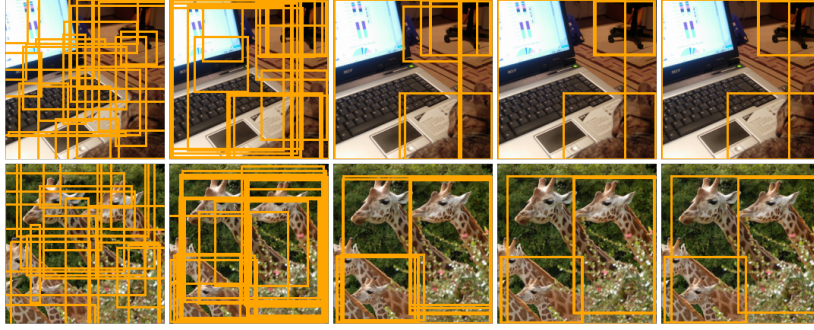


Figure 5: Visualization of the first 4 iterations of PPA using the learned proximal operator on 20 randomly initialized boxes (leftmost column). Only a few iterations are needed for the boxes to form distinctive clusters.

Table 1: Object detection results. WD_∞ (resp. $WP_\infty^{0.1}$) is the witnessed divergence (resp. precision) in (6) with $t = \infty$ (i.e. keeping all solutions), averaged over 10 trials (standard deviation $< 10^{-3}$). Precision and recall are computed with Hungarian matching as no confidence score is available for the usual greedy matching (see Section 5.5). FRCNN(.S) [Ren et al., 2015] means keeping predictions with confidence $\geq S\%$ for Faster R-CNN.

METHOD	WD_∞	$WP_\infty^{0.1}$	PRECISION	RECALL
FRCNN(.80)	0.140	0.624	0.778	0.650
FRCNN(.95)	0.162	0.589	0.887	0.515
FN	0.161	0.481	0.139	0.577
GOL	0.251	0.243	0.508	0.282
POL (OURS)	0.149	0.590	0.817	0.442

image feature vector output by ResNet-50 to a general-purpose operator network. Incorporating specialized architectures like region proposal networks into our proximal operator learning framework for object detection is an exciting future direction.

6 Conclusion

Our work provides a straightforward, effective method to learn the proximal operator of an MSO problem with varying parameters. Iterating the learned operator on randomly initialized points efficiently yields multiple optima to the MSO problem. Beyond promising results on our benchmark tasks, we see many exciting future directions that will further improve our pipeline.

A current limitation is that at test time the optimal number of iterations to apply the learned operator is not known ahead of time (see end of Appendix C.1). One way to overcome this limitation would be to train another network that estimates when to stop. This measurement can be the objective itself if the optimum is known *a priori* (e.g., sampling from level sets) or the gradient norm if objectives are smooth. One other future direction is to learn a proximal operator that adapts to multiple λ 's. This way, the user can easily experiment with different λ 's and to enable PPA with growing step sizes for super-linear convergence Rockafellar [1976, 2021]. Another direction is to study how much we can relax the assumption that \mathcal{X} is a low-dimensional Euclidean space. Our method could remain effective when \mathcal{X} is a low-dimensional submanifold of a high-dimensional Euclidean space. The challenges would be to constrain the proximal operator to a submanifold and to design a proximal term that is more suitable than the ambient ℓ^2 norm.

References

- Z. Allen-Zhu, Y. Li, and Z. Song. A convergence theory for deep learning via over-parameterization. In *International Conference on Machine Learning*, pages 242–252. PMLR, 2019.
- M. Andrychowicz, M. Denil, S. Gomez, M. W. Hoffman, D. Pfau, T. Schaul, B. Shillingford, and N. De Freitas. Learning to learn by gradient descent by gradient descent. In *Advances in neural information processing systems*, pages 3981–3989, 2016.
- A. Beck and M. Teboulle. A fast iterative shrinkage-thresholding algorithm for linear inverse problems. *SIAM journal on imaging sciences*, 2(1):183–202, 2009.
- J.-D. Benamou, G. Carlier, Q. Mérigot, and E. Oudet. Discretization of functionals involving the monge–ampère operator. *Numerische mathematik*, 134(3):611–636, 2016.
- R. Brits, A. P. Engelbrecht, and F. van den Bergh. Locating multiple optima using particle swarm optimization. *Applied Mathematics and Computation*, 189(2):1859–1883, 2007.
- C. Bunne, L. Meng-Papaxanthos, A. Krause, and M. Cuturi. Jkonet: Proximal optimal transport modeling of population dynamics. *arXiv preprint arXiv:2106.06345*, 2021.
- S. Burer, R. D. Monteiro, and Y. Zhang. Rank-two relaxation heuristics for max-cut and other binary quadratic programs. *SIAM Journal on Optimization*, 12(2):503–521, 2002.
- N. Carion, F. Massa, G. Synnaeve, N. Usunier, A. Kirillov, and S. Zagoruyko. End-to-end object detection with transformers. In *European Conference on Computer Vision*, pages 213–229. Springer, 2020.
- R. Chartrand and V. Staneva. Restricted isometry properties and nonconvex compressive sensing. *Inverse Problems*, 24(3):035020, 2008.
- L. Chen and Y. Gu. The convergence guarantees of a non-convex approach for sparse recovery. *IEEE Transactions on Signal Processing*, 62(15):3754–3767, 2014.
- T. Chen, X. Chen, W. Chen, H. Heaton, J. Liu, Z. Wang, and W. Yin. Learning to optimize: A primer and a benchmark. *arXiv preprint arXiv:2103.12828*, 2021.
- Z. Chen, A. Tagliasacchi, and H. Zhang. Bsp-net: Generating compact meshes via binary space partitioning. In *Proceedings of the IEEE/CVF Conference on Computer Vision and Pattern Recognition*, pages 45–54, 2020.
- K. Deb. Multi-objective optimization. In *Search methodologies*, pages 403–449. Springer, 2014.
- B. Deng, K. Genova, S. Yazdani, S. Bouaziz, G. Hinton, and A. Tagliasacchi. Cvxnet: Learnable convex decomposition. In *Proceedings of the IEEE/CVF Conference on Computer Vision and Pattern Recognition*, pages 31–44, 2020.
- L. Dinh, J. Sohl-Dickstein, and S. Bengio. Density estimation using real nvp. *arXiv preprint arXiv:1605.08803*, 2016.
- S. Fort, H. Hu, and B. Lakshminarayanan. Deep ensembles: A loss landscape perspective. *arXiv preprint arXiv:1912.02757*, 2019.
- C. Frogner, C. Zhang, H. Mobahi, M. Araya-Polo, and T. Poggio. Learning with a wasserstein loss. *arXiv preprint arXiv:1506.05439*, 2015.
- L. Gao, L.-X. Zhang, H.-Y. Meng, Y.-H. Ren, Y.-K. Lai, and L. Kobbelt. Prs-net: Planar reflective symmetry detection net for 3d models. *IEEE Transactions on Visualization and Computer Graphics*, 27(6):3007–3018, 2020.

- T. Garipov, P. Izmailov, D. Podoprikin, D. Vetrov, and A. G. Wilson. Loss surfaces, mode connectivity, and fast ensembling of DNNs. In *Proceedings of the 32nd International Conference on Neural Information Processing Systems*, pages 8803–8812, 2018.
- R. Ge, C. Jin, and Y. Zheng. No spurious local minima in nonconvex low rank problems: A unified geometric analysis. In *International Conference on Machine Learning*, pages 1233–1242. PMLR, 2017.
- M. X. Goemans and D. P. Williamson. Improved approximation algorithms for maximum cut and satisfiability problems using semidefinite programming. *Journal of the ACM (JACM)*, 42(6):1115–1145, 1995.
- K. Gregor and Y. LeCun. Learning fast approximations of sparse coding. In *Proceedings of the 27th International Conference on Machine Learning*, pages 399–406, 2010.
- K. He, X. Zhang, S. Ren, and J. Sun. Deep residual learning for image recognition. In *Proceedings of the IEEE conference on computer vision and pattern recognition*, pages 770–778, 2016.
- C. Hillermeier. Generalized homotopy approach to multiobjective optimization. *Journal of Optimization Theory and Applications*, 110(3):557–583, 2001.
- T. Hoheisel, M. Laborde, and A. Oberman. A regularization interpretation of the proximal point method for weakly convex functions. *Journal of Dynamics & Games*, 7(1):79, 2020.
- G. Huang, Y. Li, G. Pleiss, Z. Liu, J. E. Hopcroft, and K. Q. Weinberger. Snapshot ensembles: Train 1, get m for free. *arXiv preprint arXiv:1704.00109*, 2017.
- D. P. Huttenlocher, G. A. Klanderman, and W. J. Rucklidge. Comparing images using the hausdorff distance. *IEEE Transactions on pattern analysis and machine intelligence*, 15(9):850–863, 1993.
- H. J. Hwang, C. Kim, M. S. Park, and H. Son. The deep minimizing movement scheme. *arXiv preprint arXiv:2109.14851*, 2021.
- R. Jordan, D. Kinderlehrer, and F. Otto. The variational formulation of the fokker–planck equation. *SIAM journal on mathematical analysis*, 29(1):1–17, 1998.
- K. Kawaguchi and J. Huang. Gradient descent finds global minima for generalizable deep neural networks of practical sizes. In *2019 57th Annual Allerton Conference on Communication, Control, and Computing (Allerton)*, pages 92–99. IEEE, 2019.
- S. Kim, H.-g. Chi, X. Hu, Q. Huang, and K. Ramani. A large-scale annotated mechanical components benchmark for classification and retrieval tasks with deep neural networks. In *Proceedings of 16th European Conference on Computer Vision (ECCV)*, 2020.
- D. P. Kingma and J. Ba. Adam: A method for stochastic optimization. *arXiv preprint arXiv:1412.6980*, 2014.
- M.-J. Lai, Y. Xu, and W. Yin. Improved iteratively reweighted least squares for unconstrained smoothed ℓ_q minimization. *SIAM Journal on Numerical Analysis*, 51(2):927–957, 2013.
- J. Larson and S. M. Wild. Asynchronously parallel optimization solver for finding multiple minima. *Mathematical Programming Computation*, 10(3):303–332, 2018.
- K. Li and J. Malik. Learning to optimize. *arXiv preprint arXiv:1606.01885*, 2016.
- L. Li, M. Sung, A. Dubrovina, L. Yi, and L. J. Guibas. Supervised fitting of geometric primitives to 3d point clouds. In *Proceedings of the IEEE/CVF Conference on Computer Vision and Pattern Recognition*, pages 2652–2660, 2019.

- X. Li. Niching without niching parameters: particle swarm optimization using a ring topology. *IEEE Transactions on Evolutionary Computation*, 14(1):150–169, 2009.
- T.-Y. Lin, M. Maire, S. Belongie, J. Hays, P. Perona, D. Ramanan, P. Dollár, and C. L. Zitnick. Microsoft coco: Common objects in context. In *European conference on computer vision*, pages 740–755. Springer, 2014.
- X. Lin, H.-L. Zhen, Z. Li, Q.-F. Zhang, and S. Kwong. Pareto multi-task learning. *Advances in neural information processing systems*, 32:12060–12070, 2019.
- L. Liu, W. Ouyang, X. Wang, P. Fieguth, J. Chen, X. Liu, and M. Pietikäinen. Deep learning for generic object detection: A survey. *International journal of computer vision*, 128(2):261–318, 2020.
- M.-Y. Liu, O. Tuzel, A. Veeraraghavan, and R. Chellappa. Fast directional chamfer matching. In *2010 IEEE Computer Society Conference on Computer Vision and Pattern Recognition*, pages 1696–1703. IEEE, 2010.
- Z. Liu, Y. Lin, Y. Cao, H. Hu, Y. Wei, Z. Zhang, S. Lin, and B. Guo. Swin transformer: Hierarchical vision transformer using shifted windows. *arXiv preprint arXiv:2103.14030*, 2021.
- P. Ma, T. Du, and W. Matusik. Efficient continuous pareto exploration in multi-task learning. In *International Conference on Machine Learning*, pages 6522–6531. PMLR, 2020.
- D. Mahapatra and V. Rajan. Multi-task learning with user preferences: Gradient descent with controlled ascent in pareto optimization. In *International Conference on Machine Learning*, pages 6597–6607. PMLR, 2020.
- E. C. Marques, N. Maciel, L. Naviner, H. Cai, and J. Yang. A review of sparse recovery algorithms. *IEEE access*, 7:1300–1322, 2018.
- T. Meinhardt, M. Moller, C. Hazirbas, and D. Cremers. Learning proximal operators: Using denoising networks for regularizing inverse imaging problems. In *Proceedings of the IEEE International Conference on Computer Vision*, pages 1781–1790, 2017.
- N. J. Mitra, M. Pauly, M. Wand, and D. Ceylan. Symmetry in 3d geometry: Extraction and applications. In *Computer Graphics Forum*, volume 32, pages 1–23. Wiley Online Library, 2013.
- P. Mokrov, A. Korotin, L. Li, A. Genevay, J. Solomon, and E. Burnaev. Large-scale wasserstein gradient flows. *arXiv preprint arXiv:2106.00736*, 2021.
- J. J. Moreau. Fonctions convexes duales et points proximaux dans un espace hilbertien. *Comptes rendus hebdomadaires des séances de l’Académie des sciences*, 255:2897–2899, 1962.
- K. Museth, D. E. Breen, R. T. Whitaker, and A. H. Barr. Level set surface editing operators. In *Proceedings of the 29th annual conference on Computer graphics and interactive techniques*, pages 330–338, 2002.
- A. Navon, A. Shamsian, G. Chechik, and E. Fetaya. Learning the pareto front with hypernetworks. *arXiv preprint arXiv:2010.04104*, 2020.
- A. Neubeck and L. Van Gool. Efficient non-maximum suppression. In *18th International Conference on Pattern Recognition (ICPR’06)*, volume 3, pages 850–855. IEEE, 2006.
- I. P. Papadopoulos, P. E. Farrell, and T. M. Surowiec. Computing multiple solutions of topology optimization problems. *SIAM Journal on Scientific Computing*, 43(3):A1555–A1582, 2021.
- N. Parikh and S. Boyd. Proximal algorithms. *Foundations and Trends in optimization*, 1(3):127–239, 2014.

- J. J. Park, P. Florence, J. Straub, R. Newcombe, and S. Lovegrove. Deepsdf: Learning continuous signed distance functions for shape representation. In *Proceedings of the IEEE/CVF Conference on Computer Vision and Pattern Recognition*, pages 165–174, 2019.
- J. Podolak, P. Shilane, A. Golovinskiy, S. Rusinkiewicz, and T. Funkhouser. A planar-reflective symmetry transform for 3d shapes. *ACM Trans. Graph.*, 25(3):549–559, jul 2006. ISSN 0730-0301. doi: 10.1145/1141911.1141923. URL <https://doi.org/10.1145/1141911.1141923>.
- S. Ren, K. He, R. Girshick, and J. Sun. Faster r-cnn: Towards real-time object detection with region proposal networks. *Advances in neural information processing systems*, 28:91–99, 2015.
- R. T. Rockafellar. Monotone operators and the proximal point algorithm. *SIAM journal on control and optimization*, 14(5):877–898, 1976.
- R. T. Rockafellar. Advances in convergence and scope of the proximal point algorithm. *J. Nonlinear and Convex Analysis*, 2021.
- A. Schulz, H. Wang, E. Grinspun, J. Solomon, and W. Matusik. Interactive exploration of design trade-offs. *ACM Transactions on Graphics (TOG)*, 37(4):1–14, 2018.
- Y. Shi, J. Huang, H. Zhang, X. Xu, S. Rusinkiewicz, and K. Xu. Symmetrynet: learning to predict reflectional and rotational symmetries of 3d shapes from single-view rgb-d images. *ACM Transactions on Graphics (TOG)*, 39(6):1–14, 2020.
- V. Sitzmann, J. N. Martel, A. W. Bergman, D. B. Lindell, and G. Wetzstein. Implicit neural representations with periodic activation functions. *arXiv preprint arXiv:2006.09661*, 2020.
- G. Tsoumakas and I. Katakis. Multi-label classification: An overview. *International Journal of Data Warehousing and Mining (IJDWM)*, 3(3):1–13, 2007.
- Y. Wang and J. M. Solomon. Prnet: Self-supervised learning for partial-to-partial registration. In *33rd Conference on Neural Information Processing Systems*, 2019.
- Y. Wang, Y. Sun, Z. Liu, S. E. Sarma, M. M. Bronstein, and J. M. Solomon. Dynamic graph cnn for learning on point clouds. *Acm Transactions On Graphics (tog)*, 38(5):1–12, 2019.
- J. Xie, B. Xu, and Z. Chuang. Horizontal and vertical ensemble with deep representation for classification. *arXiv preprint arXiv:1306.2759*, 2013.
- C. Yang, Y. Gu, B. Chen, H. Ma, and H. C. So. Learning proximal operator methods for nonconvex sparse recovery with theoretical guarantee. *IEEE Transactions on Signal Processing*, 68:5244–5259, 2020.
- Y. Zhang, J. Hare, and A. Prugel-Bennett. Deep set prediction networks. *Advances in Neural Information Processing Systems*, 32:3212–3222, 2019.
- Y. Zhou, S. Liu, and Y. Ma. Nerd: Neural 3d reflection symmetry detector. In *Proceedings of the IEEE/CVF Conference on Computer Vision and Pattern Recognition*, pages 15940–15949, 2021.

A Convergence of Training

Theorem A.1. *Suppose*

1. $\Omega \subset \mathbf{R}^r$ for some $r \in \mathbf{N}_{\geq 1}$;
2. for any $\omega \in \Omega$, the objective f_ω is differentiable, ξ -weakly convex, and ∇f_ω is ζ -Lipschitz, i.e.,

$$\|\nabla f_\omega(x_1) - \nabla f_\omega(x_2)\|_2 \leq \xi \|x_1 - x_2\|_2,$$

with $\xi \leq \lambda$.

3. the activation function $\sigma(x)$ used is proper, real analytic, monotonically increasing and 1-Lipschitz, e.g., sigmoid, hyperbolic tangent.

For any $\delta > 0$, $H \geq 2$, $n \in \mathbf{N}_{\geq 1}$, assume Φ is an H -layer feed-forward neural network with hidden layer sizes m_1, \dots, m_H satisfying

$$\begin{aligned} m_1, \dots, m_{H-2} &\geq \Omega(H^2 \log(Hn^2/\delta)), \\ m_{H-1} &\geq \Omega(\log(Hn^2/\delta)), \quad m_H \geq \Omega(n). \end{aligned}$$

Let D denote the total number of weights in Φ . Then, $D = \tilde{\Omega}(n)$ and there exists a learning rate $\eta \in \mathbf{R}^D$ such that for any dataset $S = \{(x_i, \omega_i)\}_{i=1}^n$ of size n with the training loss L defined as in (3), for any $\epsilon > 0$, with probability at least $1 - \delta$ (over random Gaussian initial weights θ^0 of Φ), there exists $t = O(c_r(\lambda + \zeta)/\epsilon)$ such that $L(\Phi(\cdot, \cdot; \theta^t)) \leq L^* + \epsilon$, where $\|\theta^t\|_2^2$ stays bounded, $L^* := \min_{g \in \mathcal{X} \times \Omega \rightarrow \mathcal{X}} L(g)$ is the global minimum of the functional L , $(\theta^k)_{k \in \mathbf{N}}$ is the sequence generated by gradient descent $\theta^{k+1} := \theta^k - \eta \odot \nabla_\theta L(\Phi(\cdot, \cdot; \theta^k))$, and c_r depends on L and the initialization θ^0 .

Proof of Theorem A.1. The theorem is an application of Theorem 1 in [Kawaguchi and Huang, 2019] with the following modifications.

For $i \in [n]$, define $\ell_i(x) := f_{\omega_i}(x) + \frac{\lambda}{2} \|x - x_i\|_2^2$. To check Assumption 1 of Kawaguchi and Huang [2019], observe

$$\begin{aligned} \nabla_x \ell_i(x) &= \nabla f_{\omega_i}(x) + \lambda(x - x_i), \\ \nabla_x^2 \ell_i(x) &= \nabla^2 f_{\omega_i}(x) + \lambda I_d. \end{aligned}$$

Hence the assumption that f_{ω_i} is ξ -weakly convex implies that

$$\nabla^2 f_{\omega_i}(x) + \lambda I_d \succcurlyeq \nabla^2 f_{\omega_i}(x) + \xi I_d \succcurlyeq 0.$$

Hence ℓ_i is convex. The assumption that ∇f_{ω_i} is ζ -Lipschitz implies, for any $x_1, x_2 \in \mathcal{X} \times \Omega$,

$$\begin{aligned} \|\nabla \ell_i(x_1) - \nabla \ell_i(x_2)\|_2 &= \|\nabla f_{\omega_i}(x_1) - \nabla f_{\omega_i}(x_2) + \lambda(x_2 - x_1)\|_2 \\ &\leq \|\nabla f_{\omega_i}(x_1) - \nabla f_{\omega_i}(x_2)\|_2 + \lambda \|x_1 - x_2\|_2 \\ &\leq (\lambda + \zeta) \|x_1 - x_2\|_2. \end{aligned}$$

Hence $\nabla \ell_i$ is $(\lambda + \zeta)$ -Lipschitz.

An input vector to the neural network Φ is the concatenation $(x, \omega) \in \mathbf{R}^{d+r}$. Kawaguchi and Huang [2019] assume that the input data points are normalized to have unit length. This is not an issue, as we can scale down (x_i, ω_i) uniformly to be contained in a unit ball, then pad ω_i one extra coordinate to make $\|(x_i, \omega_i)\|_2 = 1$ for all $i \in [n]$, similar to the argument given in the footnotes before Assumption 2.1 of Allen-Zhu et al. [2019].

Lastly, we state explicit lower bounds for the layer sizes that are stated in the proof of Theorem 1 of Kawaguchi and Huang [2019] (see the paragraph below Lemma 3), instead of single bound on the total number of weights in the statement of Theorem 1. This is because Theorem 1 only states that there *exists* a network of size $\tilde{\Omega}(n)$ for which training converges, whereas *every* network satisfying the layer-wise bounds will have the same convergence guarantee. \square

B Network Architectures

The network architecture used by the operators for both POL and GOL is shown in Figure B.1. The

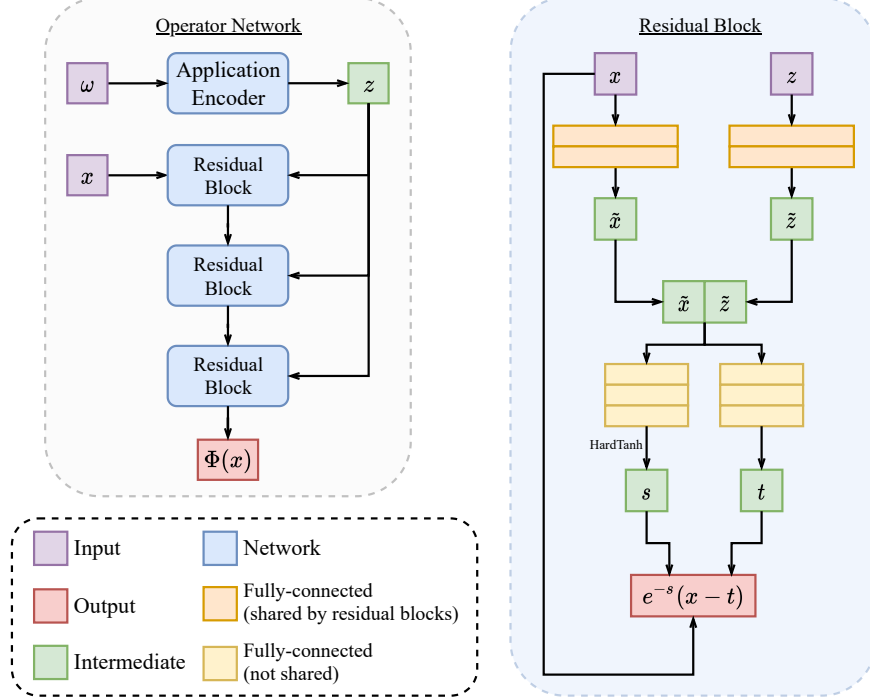


Figure B.1: Network architecture for the proximal operator (2) and the gradient operator (7). We use ReLU as the activation after all intermediate linear layers, except for predicting the scaling in the residual block, where we use HardTanh to ensure $s \in [-2, 2]$. For the shared 2-layer fully-connected network, the hidden layer sizes are 256, 128. For the 3-layer fully-connected network in each residual block, the hidden layer sizes are 128, 128, 128.

encoder for ω will be chosen depending on the application. For our conic section (5.1), sparse recovery (5.2), and max-cut (5.3) benchmarks, the encoder is just the identity map. For symmetry detection (5.4), ω is a point cloud; we use DGCNN [Wang et al., 2019]. For object detection (5.5), we use ResNet-50 [He et al., 2016]. Inspired by Dinh et al. [2016], we include both additive and multiplicative coupling in the residual blocks. At the same time, since we do not need bijectivity of the operator (and proximal operator should not be) nor access to the determinant of the Jacobian, we do not restrict ourselves to a map with triangular structure like Dinh et al. [2016]. We use 3 residual blocks for all applications, except for symmetry detection where we use 5 blocks.

Our architecture is economical: the model size (excluding the application-specific encoder) is under 2MB for all applications we consider. This also makes iterating the operators fast. Note that the application-specific encoder only needs to be run once for each test image as z in Figure B.1 can be reused.

C Detailed Results

C.1 Hyper-parameters

Unless mentioned otherwise, the following hyper-parameters are used.

Table C.1: Choices of λ for all applications considered. \mathcal{X} is the search space of solutions, and d is the dimension of the Euclidean space where we embed \mathcal{X} (so it might be greater than the intrinsic dimension of \mathcal{X}).

Application	\mathcal{X}	d	λ
conic section (5.1)	$[-5, 5]^2$	2	0.1
sparse recovery (5.2)	$[-2, 2]^8$	8	10.0
max-cut (5.3)	$(S^1)^8$	16	10.0
symmetry detection (5.4)	$S^2 \times \mathbf{R}_{\geq 0}$	4	1.0
object detection (5.5)	$[0, 1]^4$	4	1.0

In each training iteration of POL and GOL, we sample 32 problem parameters from the training dataset of Ω , and 256 of x 's from μ when computing (4) or (7). The learning rate of the operator is kept at 10^{-4} for both POL and GOL, and by default we train the operator network for 2×10^5 iterations. These are sufficient numbers of iterations for the loss to converge for both POL and GOL in most cases. Since GOL requires multiple evaluations of the gradient of the objective, it typically trains two times or more slower than POL. For the proximal weight λ of POL, we choose it based on the scale of the objective and the dimension of \mathcal{X} . See Table C.1. All training is done on a single NVIDIA RTX 3090 GPU.

For the step size η in GOL, we start with $1/\lambda$ (so same step size as POL) and then slowly increase it (so fewer iterations are needed for convergence) without degrading the metrics. For PD, we choose a step size small enough so as to not miss significant minima.

For evaluation, the number of iterations to apply the trained operators is chosen to be enough so that the objective converges. This number will be chosen separately for each application and method. By default, 1024 solutions are extracted from each method, and 1024 witnesses are sampled to compute WD_t and WP_t^δ , averaged over test dataset and over 10 trials with standard deviation provided (in most cases the standard deviation is two orders of magnitude smaller than the metrics). We filter out solutions that do not lie in \mathcal{X} .

A limitation for both POL and GOL is that when the solution set is continuous, too many applications of the learned operator can cause the solutions to collapse. We suspect this is because even with the importance sampling trick (Section 3.5), during training the operators may never see enough input that are near-optimal to learn the correct refinement needed to recover the continuous solution set. A future direction is to have another network to predict a confidence score for each $x \in \mathcal{X}$ so that at test time the user knows when to stop iterating the operator, e.g., when the objective value and its gradient are small enough; see the discussion in Section 6.

C.2 Convergence to the Proximal Operator

To verify that our method can faithfully produce the proximal operators of the objectives, we conduct the following simple experiments. We consider the function $f(x) = \|x\|_1$ for $x \in \mathcal{X} = [-1, 1]^d$. Its proximal operator $\text{prox}(x) = \arg \min_y \|y\|_1 + \|y - x\|_2^2$ is known in closed form as the shrinkage operation, defined coordinate-wise as:

$$\text{prox}(x)_i = \begin{cases} x_i - 1/2 & x_i \geq 1/2 \\ 0 & |x_i| \leq 1/2 \\ x_i + 1/2 & x_i \leq -1/2. \end{cases} \quad (13)$$

For each dimension of $d = 2, 4, 8, 16, 32$, we train an operator network Φ (Figure B.1) using (2) as the loss with learning rate 10^{-3} . Figure C.1 shows the mean-squared-error $\|\Phi(x) - \Phi^*(x)\|_2^2$ scaled by $1/d$ and averaged over 1024 samples vs. the training iterations, where Φ^* is the shrinkage operation (13). We see that the trained operator indeed converges to Φ^* in the L^2 sense, and the convergence speed is faster in smaller dimensions.

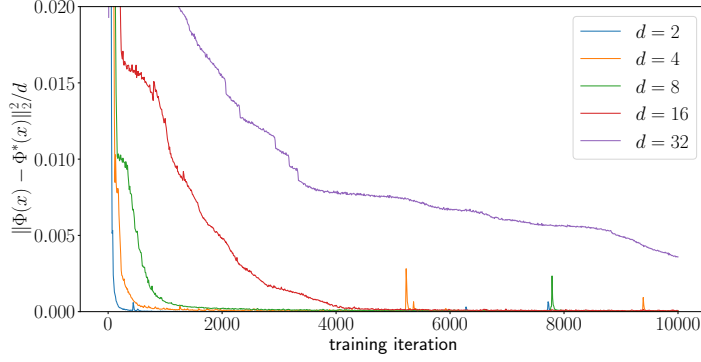


Figure C.1: Convergence to the true proximal operator of $f(x) = \|x\|_1$.

C.3 Sampling from Conic Sections

Setup. For this problem, the training dataset contains 2^{20} samples of $\omega \in \Omega$, while the test dataset has size 256. In our implementation and similarly in other benchmarks we do not store the dataset on disk, but instead generate them on the fly with fixed randomness. The ω 's are sampled uniformly in Ω . PD is run for 5×10^4 steps with learning rate 1.0. For step sizes, we choose $\lambda = 0.1$ for POL and $\eta = 1.0$ for GOL. We found that the training of GOL explodes when $\eta > 1.0$. Meanwhile, POL is able to take bigger ($1/\lambda = 10.0$) steps while staying stable during training. To obtain solutions, we use 5 iterations for POL, while for GOL we use 100 iterations since it converges slower (and more iterations won't improve the results).

Results. We visualize for the conic section problem in Figure C.2 for 16 randomly chosen $\omega \in \Omega$. In Figure C.3 we plot of δ vs. $WP_t^\delta(6)$ to quantitatively verify how good POL and GOL are at recovering the level sets, where we treat the results by PD as the ground truth. Both visually and quantitatively, we see that POL outperforms GOL. Figure C.4 compares the convergence speed when applying the learned iterative operators at test time.

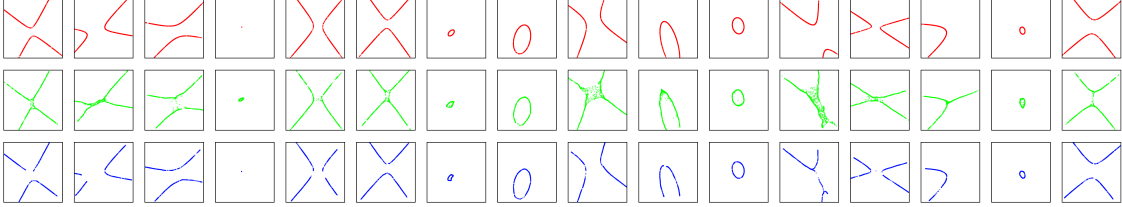


Figure C.2: Visualization of the solutions for the conic section problem. **Red** indicates the solutions by PD (Section 4.2) which we treat as ground truth. **Green** and **blue** indicate the solutions by GOL (Section 4.3) and POL (proposed method) respectively.

C.4 Non-Convex Sparse Recovery

Setup. For this problem, the training dataset contains 1024 samples of $\omega = (\alpha, p)$, while the test dataset has 128 samples. The ω 's are sampled uniformly in $\Omega = [0, 1] \times [0.2, 0.5]$. We extract 4096 solutions from each method after training. For PD, we run 5×10^5 steps of gradient step with learning rate 10^{-5} . We found that due to the highly nonconvex landscape of the problem, bigger learning rates will cause PD to miss significant local minima. For step sizes, we choose $\lambda = 10$ for POL (so this

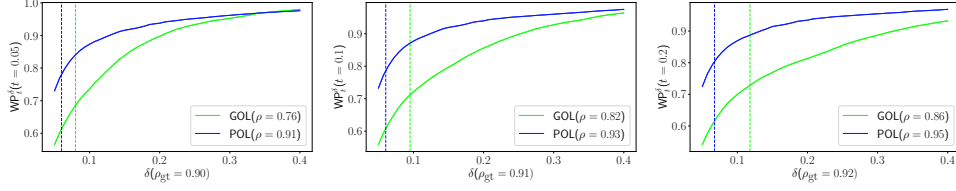


Figure C.3: The plot of δ vs. WP_t^δ for the conic section problem ($t = 0.05, 0.1, 0.2$). The vertical dashed line indicates WD_t . 50 equally spaced δ values are used to draw the plot. Here ρ_{gt} indicates the percentage of PD solutions that have objectives $\leq t$, and ρ similarly indicates the percentage of solutions for each method with objectives below t . We sample 1024 witnesses to compute WP_t^δ , averaged over 256 test problem instances. The plot is averaged over 10 trials of witness sampling (the fill-in region's width indicates the standard deviation).

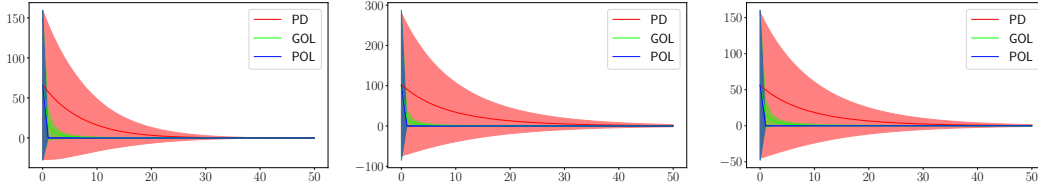


Figure C.4: Convergence speed comparison at test time for the conic section problem. For POL and GOL, the x -axis is the number of iterations used. For PD, the x -axis is the number of gradient descent steps, multiplied by 100. The horizontal axis shows the number of iterations, and the vertical axis shows the value of $f_\omega(x)$, averaged over all current solutions (fill-in region's width indicates standard deviation). The three plots shown correspond to the problem instances in the first three columns in Figure C.2. Once the operator has been trained, POL converges in less than 5 steps, while GOL converges slower (GOL is already trained with the largest step size without causing training to explode).

corresponds to step size 0.1 for backward Euler) and $\eta = 0.1$ for GOL. To obtain solutions of POL and GOL, POL requires less than 10 iterations to convergence, while for GOL around 50 iterations are needed.

Results. We show the histogram of the solutions' objective values for PD, GOL, and POL in Figure C.6 for 4 problem instances. Figure C.5 visualizes the solutions for 8 problem instances projected onto the last two coordinates. GOL fails badly in all instances. Remarkably, despite the non-convexity of the problem and the much larger step size (0.1 compared to 10^{-5}), POL yields solutions on par or better than PD when p is small. For instance, for the second and third columns in Figure C.5 (corresponding to second and third columns in Figure C.6), PD (in red) misses near-optimal solutions that POL (in blue) captures. As such the results of PD can be suboptimal, so we do not compute witness metrics here.

C.5 Rank-2 Relaxation of Max-Cut

Setup. An additional feature of (10) is that the variables are constrained to $(S^1)^8 \subset \mathbf{R}^{16}$. Hence for POL and GOL we always project the output of the operator network to the constrained set (normalizing to unit length before computing the loss or before iterating), while for PD we apply projection after each gradient step.

We generate a training dataset of 2^{20} graphs and a test dataset of 1024 graphs using the procedure described in Section 5.3: half of the graphs will be Erdős-Rényi graphs with $p = 0.5$ and the remaining half being K_8 with edge weights drawn from $[0, 1]$ uniformly. For PD, we use learning rate 10^{-4} . For step sizes of POL and GOL, we choose $\lambda = 10.0$ and $\eta = 10.0$.

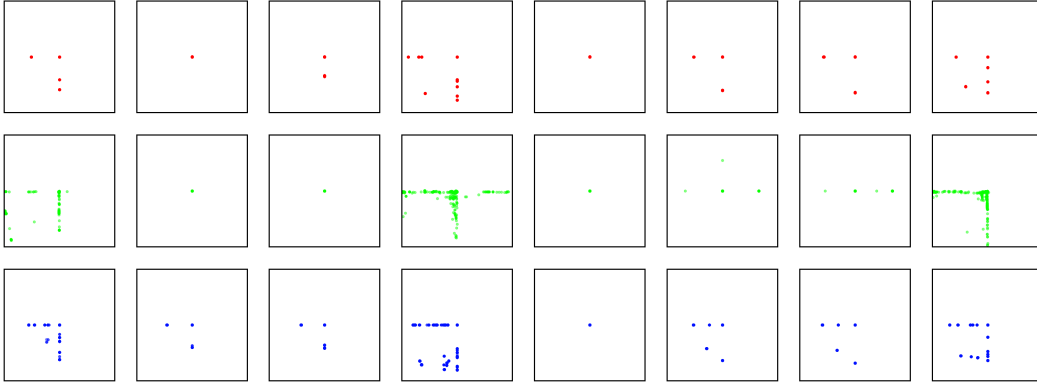


Figure C.5: Visualization of the solutions’ objective values for the conic section problem. Red indicates the solutions by PD (Section 4.2) which we treat as ground truth. Green and blue indicate the solutions by GOL (Section 4.3) and POL (proposed method) respectively.

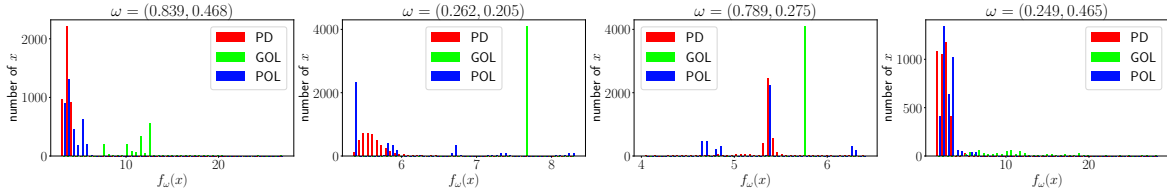


Figure C.6: Histograms of the objectives for non-convex sparse recovery on 4 problem instances. We denote $\omega = (\alpha, p)$ at the top, corresponding to a sparsity-inducing function of the form $\alpha \|x\|_p^p$.

We choose to directly feed the edge weight vector $\omega \in \mathbf{R}^{28}$ to the operator network (Appendix B). We find this simple encoding works better than alternatives such as graph convolutional networks. This is likely because $x \in \mathcal{X} = (S^1)^8$ requires order information from the encoded ω , so graph pooling operation can be detrimental for the operator network architecture. Designing an equivariant operator network that is capable of effectively consuming larger graphs is an interesting direction for future work.

Results. If a cut happens to be a local minimum of (9), then it is a maximum cut (Theorem 3.4 of Burer et al. [2002]). However, finding all the local minima of the relaxation (9) is not enough to find all max cuts as max cuts can also appear as saddle points (see the discussion after Theorem 3.4 of Burer et al. [2002]). Hence solving the MSO (10) is not enough to identify all the max cuts. Nevertheless, we can still compare POL and GOL against PD based solely on the relaxed MSO problem corresponding to the objective (10). In Figure C.7, we plot δ vs. WP_t^δ (6) to verify the quality of the solutions obtained by POL and GOL compared to PD. We see that POL more faithfully recovers the solutions generated by PD with consistently higher witnessed precision.

Empirically, we found the proposed POL can identify a diverse family of cuts. We visualize the multiple cuts obtained by POL for a number of graphs in Figure C.9. Although some cuts are not maximal, they are likely due to the relaxation (9) — not all fractional solutions correspond to a cut — and not because of the proposed method. As evident in Figure C.7, they are still very close to the local minima of (10).

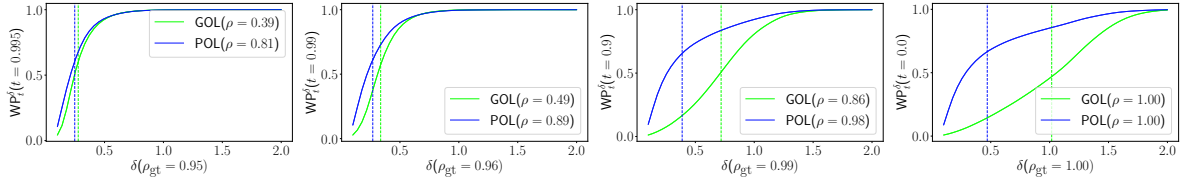


Figure C.7: The plot of δ vs. WP_t^δ for the max-cut problem. See the caption of Figure C.3 for the meaning of the symbols. As different edge weights lead to different minima values, we choose the threshold t in a relative manner: the actual threshold used will be t times the best objective value found by PD.

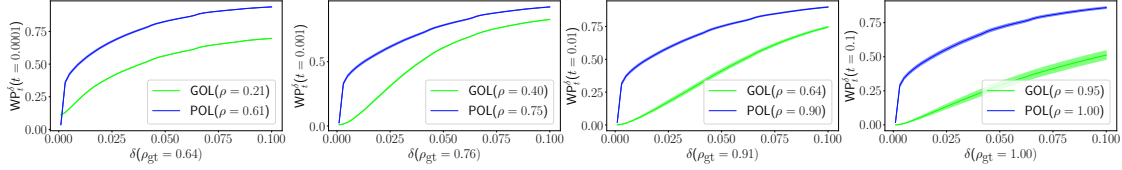


Figure C.8: The plot of δ vs. WP_t^δ for symmetry detection on the test dataset of Kim et al. [2020] ($t = 10^{-4}, 10^{-3}, 10^{-2}, 10^{-1}$). See the caption of Figure C.3 for the meaning of the various notations. We do not show WD_t as the vertical bars here because GOL's WD_t is much higher than POL's and is out of the range for the horizontal axis. We sample 1024 witnesses to compute WP_t^δ , averaged over 10 trials of witness sampling (the fill-in region's width indicates the standard deviation).

C.6 Symmetry Detection of 3D Shapes

Setup. Since the variables in (11) is constrained to $\mathcal{X} = S^2 \times \mathbf{R}_{\geq 0}$, we always project the output of the operator network to the constrained set: for $x = (n, d) \in \mathcal{X}$, we normalize n to have unit length and take absolute value of d . The same projection is applied after each gradient step in PD.

To generate training and test datasets, we use the original train/test split of the MCB dataset [Kim et al., 2020] but filtering out meshes with more than 5000 triangles and keeping up to 100 meshes per category to make the categories more balanced. During each training iteration, a fresh batch of point clouds are sampled (these are ω 's) from the meshes in the current batch. For step sizes, we choose $\lambda = 1.0$ for POL and $\eta = 10.0$ for GOL. The training of POL and GOL takes about 30 hours. For PD, we run gradient descent for 500 iterations for each model, which is sufficient for convergence.

We use the official implementation of DGCNN by Wang et al. [2019] as the encoder with the only modifications being changing the input channels to 6-dimension to consume oriented point clouds and turning off the dropout layers.

The objective (11) involves s_ω which requires point-to-mesh projection. We implemented custom CUDA functions to speed up the projection. Even so it remains the bottleneck of training. Since GOL requires multiple evaluation, it is extremely slow and can take up to more than a week. As such, we set $Q = 1$ in (7). Both POL and GOL are trained for 10^5 iterations with batch size 8. At test time iterating the operator networks does not need to evaluate the objective nor the s_ω 's; moreover, only point clouds are needed.

Results. We show the witness metrics in Figure C.8; quantitatively, POL exhibits far higher witnessed precision values than GOL. We show a visualization of iterations of PPA with the learned proximal operator in Figure C.10. In particular, our method is capable of detecting complicated discrete reflectional symmetries as well as a continuous family of reflectional symmetries for cylindrical objects.

C.7 Object Detection in Images

Setup. We use the training and validation split of COCO2017 [Lin et al., 2014] as the training and test dataset, keeping only images with at most 10 ground truth bounding boxes. For training, we use common augmentation techniques such as random resize/crop, horizontal flip, and random RGB shift, to generate a 400×400 patch from each training batch image, with batch size 32. For evaluation, we crop a 400×400 image patch from each test image. For step sizes, we choose $\lambda = 1.0$ for POL and $\eta = 1.0$ for GOL. We train both POL and GOL for 10^6 steps. This takes about 100 hours. To extract solutions, we use 100 iterations for POL (for most images it only needs 5 iterations to converge) and 1000 iterations for GOL (the convergence is very slow so we run it for a large number of iterations).

We fine-tune PyTorch’s pretrained ResNet-50 [He et al., 2016] with the following modifications. We first delete the last fully-connected layer. Then we add an additional linear layer to turn the 2048 channels into 256. We then add sinusoidal positional encodings to pixels in the feature image output by ResNet-50 followed by a fully-connected layers with hidden layer sizes 256, 256, 256. Finally average pooling is used to obtain a single feature vector for the image.

For Faster R-CNN (FRCNN), we use the pretrained model from PyTorch with ResNet-50 backbone and a regional proposal network. It should be noted that FRCNN is designed for a different task that includes prediction of class labels, and thus it is trained with more supervision (object class labels) than our method and it uses additional loss terms for class labels.

For the alternative method FN that predicts a fixed number of boxes, we attach a fully-connected layer of hidden sizes [256, 256, 80] with ReLU activation to consume the pooled feature vector from ResNet-50. The output vector of dimension 80 is then reshaped to 20×4 , representing the box parameters of 20 boxes. We use chamfer distance between the set of predicted boxes and the set of ground truth boxes as the training loss.

Results. In Table 1, we compute witness metrics and traditional metrics including precision and recall. As our method does not output confidence scores, we cannot use common evaluation metrics such as average precision. To calculate precision and recall, which normally would require an order given by the confidence scores, we instead build a bipartite graph between the predicted boxes and the ground truth, adding an edge if the Intersection over Union (IoU) between two boxes is greater than 0.5. Then we consider predictions that appear in the Hungarian max matching as true positives, and the unmatched ones false positives. Then precision is defined as the number of true positives over the total number of predictions, while recall is defined as the number of true positives over the total number of ground truth boxes. When computing metrics for POL and GOL, we run mean-shift algorithm with RBF bandwidth 0.01 to find the centers of clusters and use them as the predictions. As shown in Figure 5, the clusters formed by POL are usually extremely sharp after a few steps, and any reasonable bandwidth will result in the same clusters.

In Figure C.11, we show the detection results by our method for a large number of test images chosen at random.

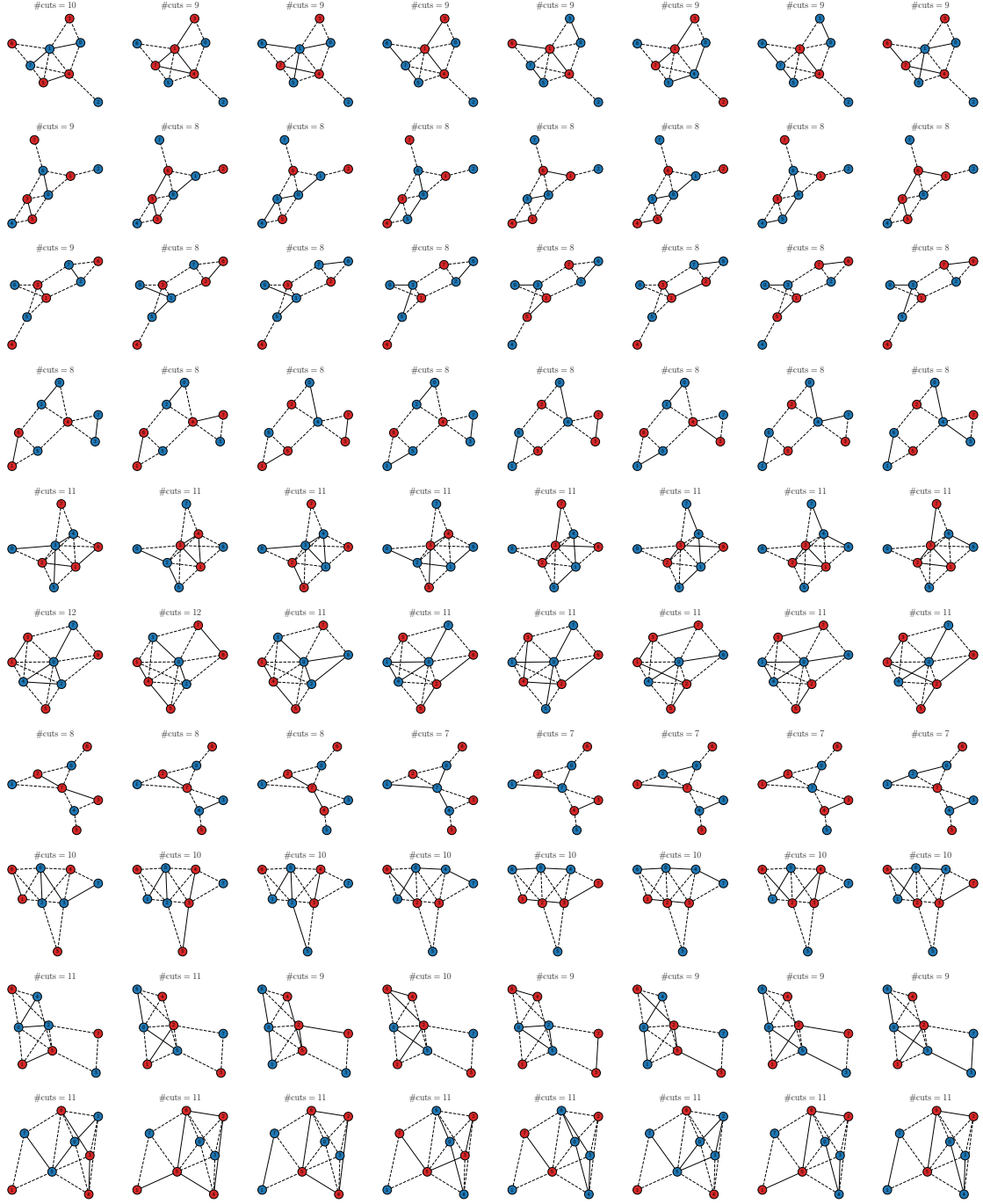


Figure C.9: Visualization of the cuts obtained by applying Goemans-Williamson-type procedure to randomly selected solutions of POL. The graphs are chosen among the ones that have at least 8 solutions uniformly at random without human intervention. Each row contains the multiple solutions for the same graph with binary weights. Two colors indicate the two vertex sets separated by the cut. Dashed lines indicate edges in the cut. For each graph we annotate the number of cuts on top. The 0th vertex is always in blue to remove the obvious duplicates obtained by swapping the two colors on each vertex.

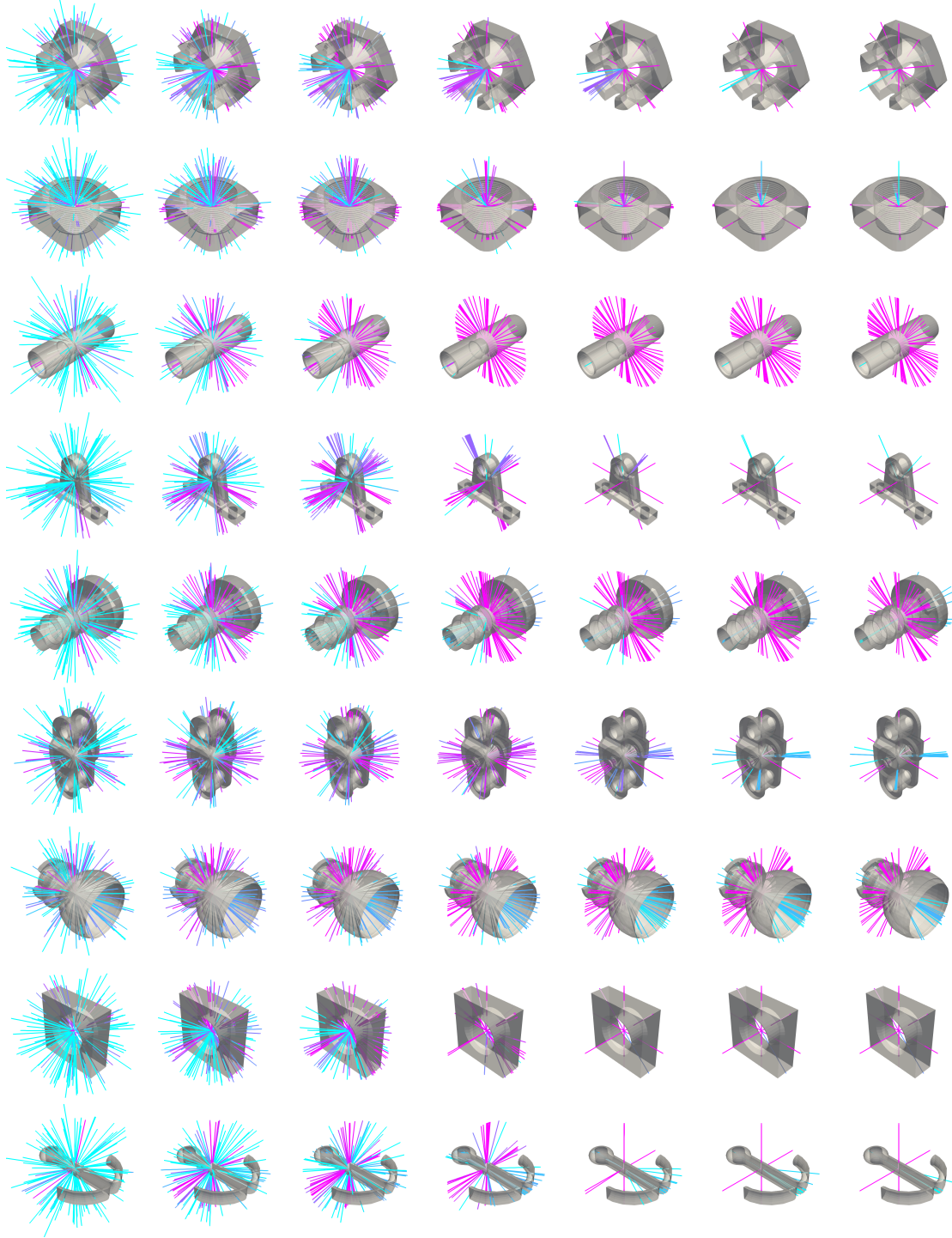


Figure C.10: Visualization of PPA with learned proximal operator on selected models from the test dataset of Kim et al. [2020]. Iterations 0, 1, 2, 5, 10, 15, 20 are shown, where the 0th iteration contains the initial samples from μ . Pink indicates lower objective value in (11), while light blue indicates higher.

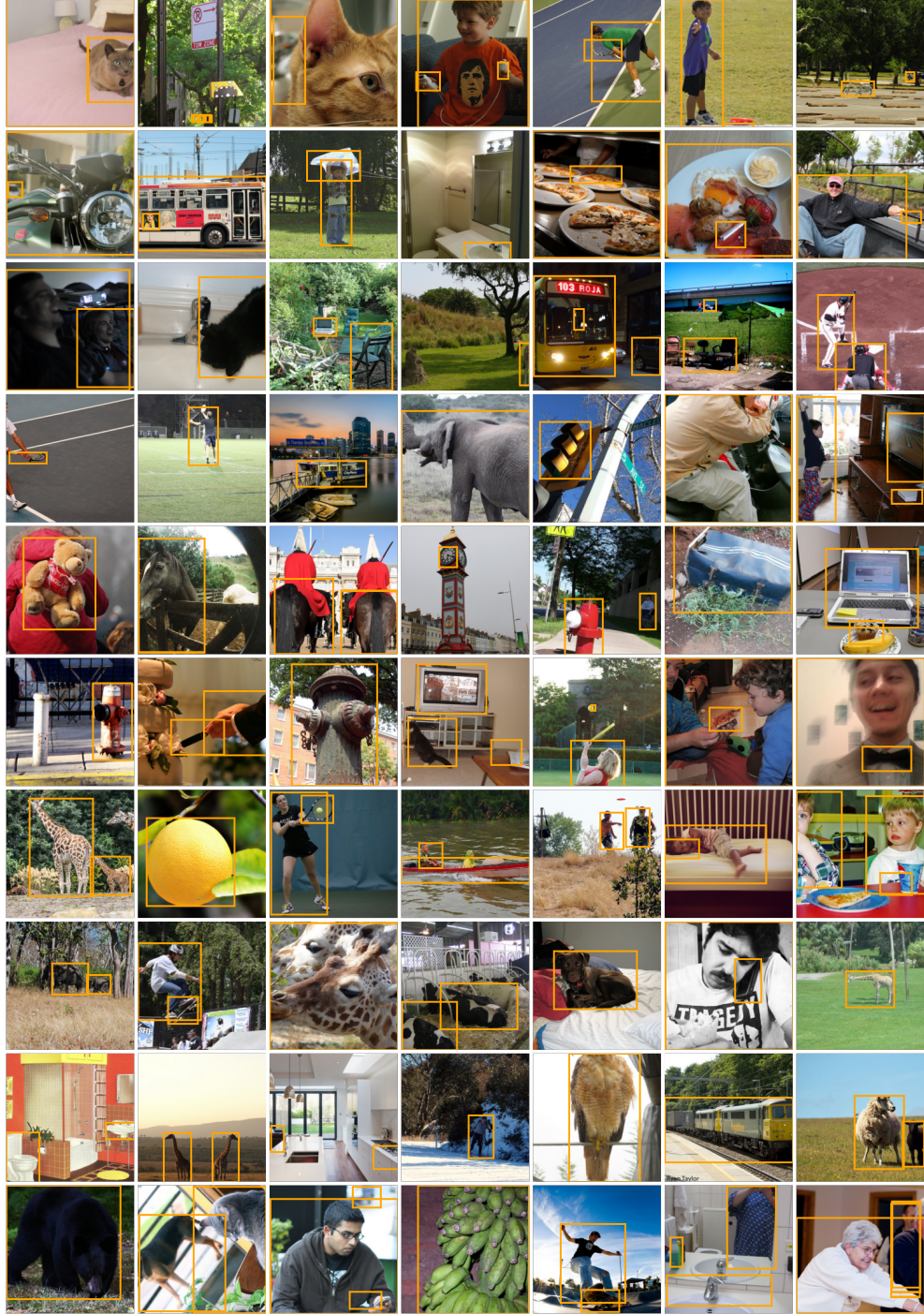


Figure C.11: Randomly selected object detection results by POL on COCO17 validation split. Each test image is 400×400 patch cropped from the original image with a random scaling by a number between 0.5 and 1. In each image we display all 1024 bounding boxes without clustering, most of which are perfectly overlapping. For some images there is a bounding box for the whole image (check if the image has an orange border). There is no class label associated with each box.